

Equatorial Plasma Bubbles Developing Around Sunrise Observed by an All-Sky Imager and GNSS Network during the Storm Time

5 Kun Wu^{1,2}, Jiyao Xu^{1,2}, Xinan Yue^{3,2}, Chao Xiong⁴, Wenbin Wang⁶, Wei Yuan^{1,2}, Chi
Wang^{1,2}, Yajun Zhu^{1,5}, Ji Luo^{1,2}

¹State Key Laboratory of Space Weather, National Space Science Center, Chinese Academy of
Sciences, Beijing, China

10 ²College of Earth Sciences, University of Chinese Academy of Sciences, Beijing, China

³Key Laboratory of Earth and Planetary Physics, Institute of Geology and Geophysics, Chinese
Academy of Sciences, Beijing, China

⁴GFZ German Research Centre for Geosciences, Telegrafenberg, 14473 Potsdam, Germany.

⁵Institute of Energy and Climate Research (IEK-7), Forschungszentrum Juelich GmbH, Juelich,
15 Germany

⁶High Altitude Observatory, National Center for Atmospheric Research, Boulder, CO, USA

Correspondence to: jyxu@spaceweather.ac.cn

20

25

Abstract. A large number of studies have shown that equatorial plasma bubbles (EPBs) occur mainly after sunset, and they usually drift eastward. However, in this paper, an unusual EPB event was simultaneously observed by an all-sky imager and the Global Navigation Satellite Systems (GNSS) network in southern China, during the recovery phase of geomagnetic storm happened on 6-8 November 2015. Observations from both techniques show that the EPBs appeared near dawn. Interestingly, the observational results show that the EPBs continued to develop after sunrise, and disappeared about one hour after sunrise. The development stage of EPBs lasted for at least about 3 hours. To our knowledge, this is the first time that the evolution of EPBs developing around sunrise was observed by an all-sky imager and the GNSS network. Our observation showed that the EPBs drifted westward, which was different from the usually eastward drifts of post-sunset EPBs. The simulation from TIE-GCM model suggest that the westward drift of EPBs should be related to the enhanced westward winds at storm time. Besides, bifurcation and merging processes of EPBs were observed by the all-sky imager in the event. Associated with the development of EPBs, increasing in the ionospheric F region peak height was also observed near sunrise, and we suggest the enhance upward vertical plasma drift during geomagnetic storm plays a major role in triggering the EPBs near sunrise.

45

1. Introduction

After sunset, plasma density depletions, also called equatorial plasma bubbles (EPBs), sometime occur in the equatorial- and low-latitude ionosphere. A large number of studies have shown that EPBs generally start to develop shortly after sunset during geomagnetic quiet periods (e.g., Weber et al., 1980; Kelley et al., 1986; Xiong et al., 2010; Wu et al., 2018). It is generally believed that the Rayleigh-Taylor instability (RTI) is a plausible mechanism to trigger the EPBs (Kelley, 2009; Makela and Otsuka, 2012). The growth rate of RTI is influenced by a number of different factors, such as the zonal electric field, neutral wind and the vertical gradient of plasma density at the bottomside of the F region or ion-neutral collision frequency, as well as the strength of magnetic

55

fields (Ott, 1978; Abdu, 2001; Burke et al, 2004). The pre-reversal enhancement (PRE) of the eastward electric field around sunset is a main reason for the development of EPBs (e.g., Fejer et al., 1999; Abdu, 2001; Kelley, 2009; Huang, 2018). Owing to the intensified eastward electric field, near magnetic equator the ionosphere is rapidly elevated to higher altitudes via $E \times B$ drifts, which is favorable for the growth of RTI at the bottomside of the ionosphere.

The EPBs are thought to extend along magnetic field lines, and can reach as high as magnetic latitudes of about $\pm 20^\circ$ (Kelley, 2009; Lühr et al., 2014). Xiong et al. (2016, 2018) suggest that EPBs have a typical zonal size of about 50 km, by using Swarm in situ electron density measurements as well as ground-based airglow imager. Although the characteristics of EPBs have been widely studied, special events, especially those occurring during geomagnetic storms, are still one of the interesting issues to be fully addressed. Some of the results showed that geomagnetic storms can affect the development of EPBs (e.g., Abdu et al., 2003; Tulasi et al., 2008; Carter et al., 2016), and in some extreme cases, the EPBs can extend to middle latitudes during intense geomagnetic storms (e.g., Sahai et al., 2009; Patra et al., 2016; Katamzi-Joseph et al., 2017; Aa et al., 2018). Moreover, in the storm time, EPBs near sunrise were occasionally observed by some instruments such as radar and satellite. Fukao et al. (2003) used observations from the Equatorial Atmosphere Radar to report EPBs near sunrise over the Indonesian region during a geomagnetic storm and suggested that the EPBs were likely associated with the geomagnetic storm. Huang et al. (2013) reported the observations of long-lasting daytime EPBs with the Communications/Navigation Outage Forecasting System (C/NOFS) satellite during a geomagnetic storm in which the EPBs were persistent from the post-midnight sector through the afternoon sector. Zhou et al. (2016) used observations from multiple low Earth orbiting satellites, like the Swarm constellation, the Gravity Recovery and Climate Experiment (GRACE) satellite, and the C/NOFS satellite, to detect the EPBs around sunrise during the St Patrick's Day storm. They suggested that the geomagnetic storm induced changes in ionospheric dynamics should be the reason for triggering the EPBs. But until now, there

85 has been no research on the occurrence characters and evolution of EPBs around sunrise using optical remote sensing, which can provide different aspects of the EPBs near sunrise.

It is well known that the EPBs usually drift eastward as reported by many studies (e.g., Pimenta et al., 2001; Martinis et al., 2003; Park et al., 2007; Taylor et al., 2013; Wu et al., 2017). However, during storm periods westward drifting EPBs have been also observed (Abdu et al., 2003; Basu et al., 2010; Santos et al., 2016). Abdu et al. (2003) reported some cases of EPBs that showed eastward drifts after sunset and later reversed to westward. Basu et al. (2010) reported that the westward drifting EPBs reached maximum velocities of about 80 - 120 m/s. Santos et al. (2016) also showed some EPBs
95 of zonal drifts reversal (eastward to westward) during a geomagnetic storm, and they suggested the reversal was caused by a vertical Hall electric field which induced by a zonal prompt penetration electric field (PPEF) in the presence of enhanced conductivity in the E region during night.

From six-year observations of airglow image located in the southern China, we found
100 only one case of EPBs starting to appear near sunrise during the storm recovery phase on 08 November 2015. The EPBs appeared before sunrise, kept developing and vanished in about 1 hour after sunrise. Unlike the quiet-time eastward drifting EPBs, the EPBs drifted westward. In the rest, we provide a detailed analysis of this event. In section 2, we give a general description of the instruments. Observational results are
105 showed in section 3. In section 4, we provide comparisons with previous studies as well as discussions. Finally, summary is given in section 5.

2. Instrumentation

2.1 All-sky imager

110 The airglow data used in this study are obtained from an all-sky imager, which is deployed at Qujing, China (Geographic: 25° N, 104° E; Geomagnetic: 15.1° N, 176° E). Its location is indicated by the red star in Figure 1, and the blue circle represents the projected regions with a radius of ~900 km (about 140° field of view (FOV)) of the all-

sky imager at an altitude of 250 km. The all-sky imager consists of a CCD detector
115 (1024 × 1024 pixel), an interference filter (630.0 nm), and a fish-eye lens (FOV of 180°).
The integration time of the all-sky imager is 3 min.

2.2 The Network of Global Navigation Satellite System (GNSS)

The GNSS data used in this study are derived from the Crustal Movement Observation
120 Network of China (CMONOC), which consists of ~260 ground GNSS receivers
covering the mainland of China. The information of these GNSS receivers has been
given in previous publications (e.g., Aa et al., 2015; Yang et al., 2016; Zheng et al.,
2016). The residuals of total electron content (TEC) was processed using the similar
125 method as that described by Ding et al. (2014). Specifically, for each arc, the relative
phase TEC was filtered using a band-pass filter. The minimum and maximum period of
the band-pass filter was 2 min and 12 min respectively. We then calculated the TEC
residual of each arc for each pierce point, which the height of each ionospheric pierce
point was about 300 km. Therefore, the TEC residual could indicate the occurrence of
130 plasma bubbles. An elevation cutoff angle of 30° is used to reduce the multi-paths
effects. Besides, to better present the structure of EPBs, the rate of TEC change index
(ROTI) was also calculated. The ROTI is the standard deviation of the TEC gradient,
which is rate of TEC change (ROT). Based on $(TEC(t+\Delta t)-TEC(t))/\Delta t$, we can get the
ROT. In the study, we used $\Delta t=30s$ to calculate the ROT and used 10 ROT to get 5 min
ROTI. Similar calculation of ROT and ROTI have already been reported and discussed
135 by many previous studies (e.g., Pi et al., 1997; Otsuka et al., 2006; Buhari et al., 2014),
we will not be described in here.

2.3 Digisonde

The digisonde ionograms are obtained from a digisonde located at Fuke, a low-latitude
140 station in the southern China (Geographic: 19.5° N, 109.1° E; Geomagnetic: 9.5° N,
178.4° W), and marked with a green dot in Figure 1. The virtual heights of the *F* layer
were manually scaled by using the SAO Explorer software.

3. Observations and Results

145 Figure 2 shows the 3-hour Kp index, the interplanetary magnetic field (IMF) Bz , $SYM-H$, AE, AU, AL and h' F at Fuke on 06-08 November 2015. To make the comparison easier with other observations, we converted the universal time to the local time (LT) at Qijing. A geomagnetic storm occurred during those days. In Figure 2(b), IMF Bz turned southward at $\sim 11:40$ LT on 07 November 2015, and reached to about -11 nT at $\sim 16:00$ LT. During the storm main phase, the $SYM-H$ had a rapid reduction from -40 nT to -100 nT. Meanwhile, the Kp index reached a value of 6; the AE and AL also reached at ~ 1500 nT and ~ -1500 nT, respectively. After $04:00$ LT on 08 November 2015, IMF Bz began to turn to north. In the storm recovery phase, the value of $SYM-H$ was back to -40 nT.

155 Figure 3 shows the time sequence of airglow images observed by the all-sky imager at Qijing from $05:15$ to $06:21$ LT on 8 November 2015. The time difference between successive images is 6 min. For each image, we removed the effects of compression and curving of the all-sky imager lens by an unwarping process (Garcia et al., 1997). All images have been mapped into a geographic range from 97° to 111° E in longitude and from 18° to 32° N in latitude. The height of the airglow layer is assumed to be at 250 km. The top of each image is to the north and the right to the east. Two EPBs, marked as “b1” and “b2”, were observed by the all-sky imager during this period. They occurred during the geomagnetic storm recovery phase.

Around $05:21$ LT, EPB “b1” appeared in the FOV of the all-sky imager. “b1” was still developing, as it extended northward and reached close to 25° N around $06:21$ LT. At $05:39$ LT, the other EPB “b2” started to appear in the FOV of the airglow imager. “b2” was also developing and expanded to about 20° N at $06:21$ LT. The two observed EPBs possibly continued to develop after $06:21$ LT, as no hints of stop can be seen in the last airglow image. However, there was no further image data after $06:21$ LT because the all-sky imager had to be shut down after sunrise. We want to pointed out that the sunrise time at Qijing was around $06:15$ LT at altitude of 250 km on that day. The far north

part of “b1” reached about 24.5°N at 06:15 LT. After 6 min, the far north of “b1” extended to about 25°N (as marked by the black horizontal line). In other words, the observational result from the all-sky imager suggested that the EPBs kept developing after sunrise.

175

Some interesting features can also be seen from Figure 3. “b1” appeared at ~105° E and “b2” appeared at ~104° E at 05:39 LT. Based on the black vertical line at 106° E, we can clearly see that the two EPBs drifted from east to west. Besides, bifurcation and merging processes of EPB “b1” were also observed. After 05:45 LT, a bifurcation process occurred in “b1”. The lower latitude portion of “b1” moved further to the westward. An obvious cleft occurred at ~19° N of “b1” near 06:03 LT. More interesting is the fact that a merging process occurred in the two bifurcation portions of “b1” during its later development period. After ~06:03 LT, the upper portion of “b1” began to connect to the lower portion of “b1” and they merged/combined together into one EPB after 06:15 LT. The bifurcation and merging processes are more obvious in the red rectangles of Figure 3, which is indicated by the red arrow in each image.

180

185

Figure 4 shows a series of TEC residuals over 10°-50°N and 80°-130°E during 04:30-08:20 LT on 08 November 2015. The adjacent imaging is in 10 min intervals. At about 04:40 LT, some TEC depletions, which occurred to the south and west of the location of all-sky imager, appeared at ~115°E (~24°N), and began to develop. About 05:30 LT, some additional EPBs appeared at ~105°E (~20°N), and they were also developing. EPBs in the two regions kept developing until they disappeared. Owing to the FOV of the all-sky imager, the EPBs outside the ~115°E region were not observed.

190

In order to provide much more detailed comparison between the all-sky imager and TEC measurements, we give local time variation of the absolute TEC after 05:15 LT (Figure 5) which corresponding geographical area of airglow imaging. In Figure 5, the TEC depletions at ~105° E appeared near 05:30 LT, which correspond to EPB “b1” and “b2” observed by the all-sky imager. And after ~07:45 LT, those TEC depletions disappeared. For a better representation, we showed ROTI variations which correspond geographical area and time of each airglow imaging of Figure 3. In Figure 6, the ROTI

195

200

enhancement at $\sim 105^\circ$ E also correspond to EPB “b1” and “b2” observed by the all-sky imager near 05:30 LT. The ROTI enhancement move away from the 106° E with time (The black vertical line represents the 106° E in Figure 6), which is consistent with the movement of EPBs observed by the airglow imager. Meanwhile, the northernmost part of the ROTI enhancement expanded to $\sim 25^\circ$ N at 06:21 LT (The black horizontal line represents the 25° N in Figure 6), which also agreed well with the observations of the all-sky imager. Interestingly, In Figure 4, TEC residuals show that the northernmost of EPBs of $\sim 105^\circ$ E extended beyond 25° N after 06:20 LT. We can see that the northernmost of them reached about 28° N at 07:10 LT. In other words, TEC variations show that those depletions were still existence after 06:21 LT, and kept developing after sunrise, but vanished near $\sim 08:00$ LT. These observational results shown that the life time of those EPBs exceeds 3 hours.

4. Discussion

In this study we showed an special event of EPBs which was simultaneously observed by the all-sky imager and the ground GNSS network in the south China. One interesting feature is that the EPBs started to appear near sunrise hours. Afterward, they kept developing until they totally vanished. During their life time, the EPBs moved from east to west. Those EPBs occurred in the recovery phase of the geomagnetic storm, which indicates that the prompt penetration electric fields (PPEF) and disturbance dynamo, as well as disturbed neutral wind circulation may play an import role in triggering the EPBs.

The drift velocities of EPBs were shown in Figure 7. We used the cross sections (keogram) (Figures 7 (a), (c), and (e)) of the airglow images to separately calculate meridian velocities (Figure 7(b)) of “b1” and zonal velocities of “b1” at $\sim 22^\circ$ N (Figure 7(d)) and $\sim 19^\circ$ N (Figure 7(f)) geographical latitudes. Figure 7(a) illustrates the N-S cross sections (between 104° E and 105° E) of the airglow images shown in Figure 3. Figure 7(c) illustrates the W-E cross sections (between 21.5° N and 22° N) of the airglow images, and Figure 7(e) illustrates the W-E cross sections (between 18.5° N and 19° N). We separately calculated poleward and zonal velocities of “b1” based on the position

of it changed over time in Figure 7(a), Figure 7(c) and Figure 7(e). The initial poleward and zonal velocities of “b1” were about 200 m/s and 60 m/s, respectively. Horizontal drift of EPB is also an important issue, which is often related to the background zonal plasma drift (Fejer et al., 2005; Eccles, 1998). The westward motion of the F-region should be caused by the ionospheric dynamo process in the early morning (Kil et al., 235 2000; Sheehan and Valladares, 2004). The drift direction of background zonal plasma drift has a reversal (eastward to westward) near dawn (Fejer et al., 2005). Huang and Roddy. (2015) also found the drift velocity of EPBs was eastward at night and reverses to westward near dawn by using data from C/NOFs and they showed enhanced geomagnetic activities caused a westward EPB drift in the nighttime through 240 disturbance dynamo process. In our case, all EPBs emerged after 05:00 LT. The background plasma should drift westward during the early morning hours. So, it could partly explain why the observed EPBs drifted westward. In addition, the disturbed westward neutral winds can also contribute to the westward drifting of EPBs. Xiong et al. (2015) found that the disturbance winds were mainly towards westward at low 245 latitudes, most prominent during early morning hours. Abdu et al. (2003) found that the westward drift of an EPB was most likely caused by westward zonal winds during a geomagnetic storm. Makela et al. (2006) found that the eastern wall of EPBs can become unstable due to the westward and equatorward neutral winds associate with wind surges. When the wind blow westward, and thus the wind-induced Pedersen 250 current flows downward, gradient-drift instability can occur at the eastern wall of EPB, where the plasma density gradient is eastward. So, secondary instabilities are more likely to occur at eastern wall of EPBs. In Figure 3, a sub-branch of dark bands first occurred at the eastern wall of “b1”, indicated secondary instabilities developed at the 255 eastern edge, most likely due to the westward disturbance winds.

In Figure 8, we used the Thermosphere-Ionosphere-Electrodynamics General Circulation Model (TIE-GCM) to simulate the horizontal winds on 08 November 2015 under magnetically active conditions, and the latitude versus longitude distribution of zonal wind velocities are shown at different times. The winds at 250 km are shown, and

260 the spatial coverage has been confined to 0° - 40° N latitude and 90° - 120° E longitude. The dashed rectangles represent the location of “b1” and “b2” at different times. In Figure 8, we can see that the horizontal winds at low latitudes are mainly westward, which is consistent with the motion of EPBs in this case. As already discussed above, the westward drift of those EPBs is possibly caused by the westward disturbance winds.

265 Besides, the zonal winds computed from TIE-GCM shown in Figure 8 are smaller than the zonal drifts of EPBs shown in Figure 7. This is because zonal drift value of EPBs was controlled by background zonal winds and ionospheric electric field (Haerendel et al., 1992; Eccles, 1998). The value differences between simulation and zonal drifts of EPBs should be influenced by ionospheric electric field. Besides, The difference

270 between the model simulated background zonal winds and the derived zonal drifts of EPBs from airglow images is possibly due to that the model simulation provide mainly reflect a general trend of the wind, but not the exact wind velocity in reality.

As reported, most of the EPBs start to occur at pre-midnight hours. There were a very limited number of studies that used data from radar or satellite to report the occurrence

275 of EPB close to sunrise hours (e.g., Fukao et al., 2003; Huang et al., 2013; Zhou et al., 2016). However, until now, there has been no observation result of EPBs around sunrise using optical remote sensing. In fact, it is very difficult to observe EPB near sunrise by an all-sky imager. Often, EPBs start to develop shortly after sunset and vanish before sunrise. Even though some EPBs occur around sunrise in their initial stage, they

280 disappear when they drift eastward into the daytime. And almost no report shows that the EPBs still kept developing after sunrise. In our case, the developing EPB was first observed at about 05:30 LT (near dawn) by both the all-sky imager and the GNSS network. The local time variation of absolute TEC showed that EPBs existed after sunrise and they disappeared after 07:45 LT. Our observational results show that they

285 kept developing after sunrise, and vanished about one hour after sunrise. Those EPBs should be occurred near sunrise, which is different from post-sunset EPBs. Their development stages lasted for at least about 3 hours.

In the rest, we try to explain why the EPBs occurred near sunrise. During the storm

time, disturbance winds can affect the low-latitude ionospheric electrodynamics as well
290 as the zonal drift of an EPB. The DDEF caused by storm will drive plasma drift to move
upward during nighttime (Blanc and Richmond, 1980). Meanwhile, a number of studies
found that high latitude electric fields can penetrate into the middle and low-latitude
ionosphere as PPEF when IMF B_z turns southward or northward (Kelley et al., 1979;
Scherliess and Fejer, 1997; Cherniak and Zakharenkova, 2016; Carter et al., 2016; Patra
295 et al., 2016; Katamzi-Joseph et al., 2017). For the storm event, after IMF B_z turned
southward at ~12:00 LT 07 November 2015, there was long duration and high AE in
storm time. A DDEF should be present at recovery phase of storm time. And it reversed
ambient electric field from westward to eastward near sunrise, which enhanced height
of bottomside of the ionosphere F -region. Meanwhile, the northward turning of IMF B_z
300 at ~04:00 LT 08 November 2015 caused over-shielding electric field, which produced
an eastward PPEF into the low-middle latitude ionosphere. The eastward electric field
also moved the F region ionosphere to higher altitudes via vertical $E \times B$ drifts. In Figure
2(e), the increased height of bottomside of the ionosphere F -region can be seen at Fuke.
In low latitude region, one of the necessary conditions for the generation of EPBs is
305 that the F layer should be uplifted to a higher altitude, where the RTI becomes unstable
and forms EPBs. The F layer height is largely determined by the eastward field via the
vertical $E \times B$ drift (Dabas et al., 2003).

In this study, EPBs were initially observed by the all-sky imager at about 05:15 LT. We
think that only a portion of the EPBs were observed in our study, as EPB usually extend
310 along the whole magnetic flux-tube. It also means that the EPBs should possibly occur
before 05:15 LT at equatorial latitude. But due to the lack of observations at equator,
we cannot provide direct evidence about their generation. However, as shown in our
Figure 9, we also found that spread F began to appear in the ionograms from the
digisonde at Fuke after 05:15 LT, which indicates that those EPBs occurred in the region
315 of southeastern Qujing (Note that Fuke is to the southeast of Qujing). Bottomside of the
ionospheric F -region at Fuke was rapidly elevated from ~250 km to ~290 km near
sunrise on 08 November 2015. The rapidly elevated height of the ionosphere can cause

stronger RTI at the bottom of the ionosphere F-region, which is beneficial to the formation of EPB. The initial occurring time of EPBs of this case should be during this
320 time. Unfortunately, we do not have more observations in the southeast of Fuke. We used the TIE-GCM to simulate the height of hmF2 at lower latitude on 08 November 2015. Figure 10 shows the hmF2 as a function of longitude and latitude at different times. The model results plotted are in a geographic range from 0° to 40° N in latitude and from 90° to 120° E in longitude. In Figure 10, we can see that hmF2 southeast of
325 (the dashed rectangles) Qujing was rapidly elevated to higher altitudes near sunrise. In other words, when the IMF B_z turned northward at about 04:00 LT, the ionosphere in some regions southeast of Qujing could be rapidly elevated to higher altitudes at this time. Those EPBs occurred in the same time period as highlighted by the green rectangular area in Figure 2. Previous studies have reported that the occurrence of the
330 dawn enhancement in the equatorial ionospheric vertical plasma drift (Zhang et al., 2015, 2016). They found that the enhancement of the ionospheric vertical plasma drift occurs around dawn. They suggested that the vertical plasma drifts can be enhanced near sunrise in a way similar to the PRE near sunset. Fejer et al. (2008) found that the nighttime disturbance dynamo drifts are upward, and have the largest values near
335 sunrise. In our case, the model simulations and observations both show an increasing of the height of the ionosphere around sunrise. The enhancement of low-latitude ionospheric vertical plasma drift caused by DDEF and PPEF associated with the geomagnetic storm should play a vital role in triggering those EPBs. Our results also provide evidence of the enhancement of low-latitude ionospheric vertical plasma drift
340 around sunrise, which should be the main reason of the EPBs generation near dawn.

In addition, some interesting features of EPBs are also shown in Figure 3 in that the EPBs showed also bifurcation and merging processes. Merging phenomenon of EPBs has been studied by some researchers (Huang et al., 2012; Huba et al., 2015; Narayanan et al., 2016; Wu et al., 2017). However, there is no study to report that bifurcation first
345 and merging later occur in evolution of one EPBs. In Figure 7(f), at latitude of 19°N, the zonal velocity of “b1” was about 60-70 m/s between 05:20 LT and 06:15 LT.

However, at the latitude of 22°N (Figure 7(d)), the zonal velocity of “b1” was decreased from about 70 m/s to about 50 m/s between 05:20 LT and 05:45 LT. After 05:45 LT, its velocity began to increase from ~50 m/s to ~70 m/s from 05:45 LT to 06:00 LT. Then, it kept a velocity of ~70 m/s. Owing to the fact that the zonal velocity at higher latitudes was smaller than that at low latitudes before 05:45 LT, “b1” had a bifurcation process of EPBs during this period. After 05:45 LT, the zonal velocity at higher latitude was bigger than that at lower latitude, “b1” exhibited a merging process of EPBs after 06:03 LT. The above results indicate that the bifurcation and merging processes of EPBs should be caused by the different drift velocities of the background plasma at different latitudes.

5. Summary

In this paper, a special EPB event was observed by an all-sky imager and the GNSS network in the southern China. The evolution processes and characteristics of those EPBs were studied in detail. Our main findings are summarized as below:

- (1) The observed EPBs on 08 November 2015 emerged before sunrise and kept developing. They dissipated at about one hour after sunrise (~ after 08:00 LT) and the development stage lasted for at least about 3 hours. The evolution of EPBs developing around sunrise was observed for the first time by an all-sky imager and the GNSS network.
- (2) They occurred in the recovery phase of a geomagnetic storm. The enhancement of background ionospheric vertical plasma drift was also observed near sunrise. The rapid uplift of the ionospheric caused by the geomagnetic storm should be the main reason for triggering the EPBs.
- (3) During the development, the EPBs drifted westward rather than eastward, The TIE-GCM simulation suggested that the westward drift of EPB is related to the westward disturbance winds.
- (4) The EPB exhibited also bifurcation and merging processes during its development.

Data availability. The airglow and digisonde data used in this work are available at

<http://data.meridianproject.ac.cn/>. The airglow data used in this study also can be obtained by contacting the corresponding author. The GNSS data used in this work is from the Crustal Movement Observation Network of China (CMONOC, <http://neiscn.org/>). The IMF, AE, AL, AU, KP, and SYM/H data are obtained from the
380 CDAWeb (<https://cdaweb.sci.gsfc.nasa.gov/>) and the WDC for geomagnetism at Kyoto University (<https://wdc.kugi.kyoto-u.ac.jp/>).

Author contributions. KW and JX conceived the study, processed airglow data, analysed the data and discussed the results, and led the writing the manuscript. XY
385 provided the GNSS data, and assisted in discussing the results. CX assisted in discussing the results of the study and reviewing the manuscript. WW provided the TIE-GCM simulations and reviewing the manuscript. WY, CW, YZ and JL assisted in reviewing the manuscript.

390 *Competing interests.* The authors declare that they have no conflict of interest.

Acknowledgements. We acknowledge the use of data from the Chinese Meridian Project. This work was supported by the Open Research Project of Large Research Infrastructures of CAS – “Study on the interaction between low/mid-latitude
395 atmosphere and ionosphere based on the Chinese Meridian Project” and the Chinese Meridian Project, and the National Natural Science Foundation of China (41831073 and 41674152). We acknowledge the use of GNSS data from the Crustal Movement Observation Network of China (CMONOC, <http://neiscn.org/>) and the data could be obtained upon request. We thank H. Liu from Macao University of Science and
400 Technology for processing the GNSS data. The development of the TEC process program is supported by the Science and Technology Development Fund, Macau SAR (File no. 001/2016/AFJ and 0001/2019/A1). The National Center for Atmospheric Research is sponsored by the National Science Foundation.

Review statement. This paper was edited by Keisuke Hosokawa and reviewed by Yuichi Otsuka and two anonymous referees.

405 **References**

- Aa, E., Huang, W., Yu, S., Liu, S., Shi, L., Gong, J., Chen, Y and Shen, H.: A regional ionospheric tec mapping technique over china and adjacent areas on the basis of data assimilation, *J. Geophys. Res.*, 120, 5049-5061, <https://doi.org/10.1002/2015JA021140>, 2015.
- 410 Aa, E., Huang, W., Liu, S., Ridley, A., Zou, S., Shi, L., Chen, Y., Shen, H., Yuan, T., Li, J., and Wang, T.: Midlatitude plasma bubbles over China and adjacent areas during a magnetic storm on 8 September 2017, *Space Weather.*, 16, 321–331, <https://doi.org/10.1002/2017SW001776>, 2018.
- Abdu, M. A.: Outstanding problems in the equatorial ionosphere–thermosphere electrodynamics relevant to spread f, *J. Atmos. Sol. Terr. Phys.*, 63, 869-884, [https://doi.org/10.1016/S1364-6826\(00\)00201-7](https://doi.org/10.1016/S1364-6826(00)00201-7), 2001.
- Abdu, M. A.: Magnetospheric disturbance induced equatorial plasma bubble development and dynamics: A case study in Brazilian sector, *J. Geophys. Res.*, 108, A12, <https://doi.org/10.1029/2002ja009721>, 2003.
- 420 Basu, S., Basu, S., MacKenzie, E., Bridgwood, C., Valladares, C. E., Groves, K. M., and Carrano, C.: Specification of the occurrence of equatorial ionospheric scintillations during the main phase of large magnetic storms within solar cycle, *Radio Science.*, 45, RS5009, <https://doi.org/10.1029/2009RS004343>, 2010.
- Blanc, M., and Richmond, A. D.: The ionospheric disturbance dynamo, *J. Geophys. Res.*, 85, A4, <https://doi.org/10.1029/JA085iA04p01669>, 1980.
- 425 Buhari, S. M. , Abdullah, M. , Hasbi, A. M. , Otsuka, Y. , Yokoyama, T. , & Nishioka, M.: Continuous generation and two - dimensional structure of equatorial plasma bubbles observed by high - density gps receivers in southeast asia, *J. Geophys. Res.*, 119, 12, <https://doi.org/10.1002/2014JA020433>, 2014.
- 430 Burke, W. J., Gentile, L. C., Huang, C. Y., Valladares, C. E., and Su, S. Y.: Longitudinal

- variability of equatorial plasma bubbles observed by dmsp and rocsat-1, *J. Geophys. Res.*, 109, 17, <https://doi.org/10.1029/2004JA010583>, 2004.
- Carter, B. A., Yizengaw, E., Pradipta, R., Retterer, J. M., Groves, K., Valladares, C., Caton, R., Bridgwood, C., Norman, R., and Zhang, K.: Global equatorial plasma
 435 bubble occurrence during the 2015 St. Patrick's day storm, *J. Geophys. Res.*, 121, 894-905, <https://doi.org/10.1002/2015JA022194>, 2016.
- Cherniak, I., and Zakharenkova, I.: First observations of super plasma bubbles in Europe, *Geophys. Res. Lett.*, 43, 137–11,145, <https://doi.org/10.1002/2016GL071421>, 2016.
- 440 Dabas, R. S., Singh, L., Lakshmi, D. R., Subramanyam, P. , Chopra, P. , and Garg, S. C.: Evolution and dynamics of equatorial plasma bubbles: relationships to exb drift, postsunset total electron content enhancements and equatorial electrojet strength, *Radio Science.*, 38, 1075, <https://doi.org/10.1029/2001RS002586>, 2003.
- Ding, F., Wan, W., Mao, T., Wang, M., Ning, B., Zhao, B., and Xiong, B.: Ionospheric
 445 response to the shock and acoustic waves excited by the launch of the Shenzhou 10 spacecraft, *Geophys. Res. Lett.*, 41, 3351–3358, <https://doi.org/10.1002/2014GL060107>, 2004.
- Eccles., V. J.: A simple model of low-latitude electric fields, *J. Geophys. Res.*, 103, 26699-26708, <https://doi.org/10.1029/98JA02657>, 1998.
- 450 Fukao, S., Ozawa, Y., Yamamoto, M., and Tsunoda, R. T.: Altitude extended equatorial spread F observed near sunrise terminator over Indonesia, *Geophys. Res. Lett.*, 30, 2137, <https://doi.org/10.1029/2003GL018383>, 2003.
- Fejer, B. G., Scherliess, L., and Paula, E. R. D.: Effects of the vertical plasma drift velocity on the generation and evolution of equatorial spread-f, *J. Geophys. Res.*, 104, 859-869, <https://doi.org/10.1029/1999JA900271>, 1999.
- 455 Fejer, B. G., Souza, J. R., Santos, A. S., and Pereira, A. E. C.: Climatology of F₂ region zonal plasma drifts over Jicamarca, *J. Geophys. Res.*, 110, A12310, <https://doi.org/10.1029/2005JA011324>, 2005.
- Fejer, B. G., Jensen, J. W., and Su, S.-Y.: Seasonal and longitudinal dependence of

- 460 equatorial disturbance vertical plasma drifts, *Geophys. Res. Lett.*, 35, 20,
<https://doi.org/10.1029/2008gl035584>, 2008.
- Garcia, F. J., Taylor, M. J., and Kelley, M. C.: Two-dimensional spectral analysis of
mesospheric airglow image data, *Applied Optics.*, 36, 7374, <https://doi.org/10.1364/AO.36.007374>, 1997.
- 465 Haerendel, G., Eccles, J. V., and Çakir, S.: Theory for modeling the equatorial evening
ionosphere and the origin of the shear in the horizontal plasma flow, *J. Geophys.
Res.*, 97, 1209–1223, <https://doi.org/10.1029/91JA02226>, 1992.
- Huang, C.-S., J. M. Retterer, O. de La Beaujardiere, P. A. Roddy, D. E. Hunton, J. O. Ballenthin,
and R. F. Pfaff.: Observations and simulations of formation of broad plasma depletions
470 through merging process, *J. Geophys. Res.*, 117, A02314,
<https://doi.org/10.1029/2011JA017084>, 1, 2012.
- Huang, C. S. , Beaujardiere, O. D. L. , Roddy, P. A. , Hunton, D. E. , Ballenthin, J. O. ,
and Hairston, M. R.: Long-lasting daytime equatorial plasma bubbles observed by
the c/nofs satellite, *J. Geophys. Res.*, 118, 2398-2408,
475 <https://doi.org/10.1002/jgra.50252>, 2013.
- Huang, C. S. , and Roddy, P. A.: Effects of solar and geomagnetic activities on the zonal
drift of equatorial plasma bubbles, *J. Geophys. Res.*, 121, 628-637,
<https://doi.org/10.1002/2015JA021900>, 2015.
- Huang, C. S.: Effects of the postsunset vertical plasma drift on the generation of
480 equatorial spread f, *Progress in Earth and Planetary Science.*, 5, 3,
<https://doi.org/10.1186/s40645-017-0155-4>, 2018.
- Huba, J. D., T.-W. Wu, and J. J. Makela.: Electrostatic reconnection in the ionosphere, *Geophys.
Res. Lett.*, 42, 1626–1631, <https://doi.org/10.1002/2015GL063187>, 2015.
- Katamzi-Joseph, Z. T., Habarulema, J. B., and Hernández-Pajares, M.: Midlatitude
485 postsunset plasma bubbles observed over Europe during intense storms in April
2000 and 2001, *Space Weather.*, 15, 1177–1190,
<https://doi.org/10.1002/2017SW001674>, 2017.
- Kelley, M. C., Fejer, B. G., and Gonzales, C. A.: An explanation for anomalous

- equatorial ionospheric electric fields associated with a northward turning of the
490 interplanetary magnetic field, *Geophys. Res. Lett.*, 6, 301-304,
<https://doi.org/10.1029/GL006i004p00301>, 1979.
- Kelley, M. C., Labelle, J., Kudeki, E., Fejer, B. G., Basu, S., Baker, K. D., Hanuise, C.,
Argo, P., Woodman, R.F., Swartz, W. E., Farley, D., and Meriwether, J.: The
Condor Equatorial Spread F Campaign: Overview and results of the large-scale
495 measurements, *J. Geophys. Res.*, 91, 5487–5503,
<https://doi.org/10.1029/JA091iA05p05487>, 1986.
- Kelley, M. C.: *The Earth's Ionosphere: Plasma Physics and Electrodynamics*, San
Diego, CA: Academic, 2009.
- Kil, H., Kintner, P. M., De Paula, E. R., and Kantor, I. J.: Global positioning system
500 measurements of the ionospheric zonal apparent velocity at cachoeira paulista in
brazil, *J. Geophys. Res.*, 105, 5317-5327, <https://doi.org/10.1029/1999JA000244>,
2000.
- Lühr H., Xiong, C., Park, J., and Rauberg, J.: Systematic study of intermediate scale
structures of equatorial plasma irregularities in the ionosphere based on CHAMP
505 observations, *Front Phys.*, 2, 15, <https://doi.org/10.3389/fphy.2014.00015>, 2014.
- Makela, J. J., Kelley, M. C., and Nicolls, M. J.: Optical observations of the development
of secondary instabilities on the eastern wall of an equatorial plasma bubble, *J.*
Geophys. Res., 111, <https://doi.org/10.1029/2006JA011646>, 2006.
- Makela, J. J., and Otsuka, Y.: Overview of Nighttime Ionospheric Instabilities at Low-
510 and Mid-Latitudes: Coupling Aspects Resulting in Structuring at the Mesoscale,
Space Science Reviews., 168, 419, <https://doi.org/10.1007/s11214-011-9816-6>,
2012.
- Martinis, C., Eccles, J. V., Baumgardner, J., Manzano, J., and Mendillo, M.: Latitude
dependence of zonal plasma drifts obtained from dual - site airglow
515 observations, *J. Geophys. Res.*, 108, <https://doi.org/10.1029/2002JA009462>, 2003.
- Narayanan, V. L., S. Gurubaran, and K. Shiokawa.: Direct observational evidence for the
merging of equatorial plasma bubbles, *J. Geophys. Res. Space Physics*, 121, 7923–7931,

<https://doi.org/10.1002/2016JA022861>, 2016.

- Ott, E.: Theory of Rayleigh-Taylor bubbles in the equatorial ionosphere, *J. Geophys. Res.*, 83, 2066, <https://doi.org/10.1029/JA083ia05p02066>, 1978.
- 520 Otsuka, Y., T. Aramaki, T. Ogawa, and A. Saito.: A statistical study of ionospheric irregularities observed with a GPS network in Japan, in *Recurrent Magnetic Storms: Corotating Solar Wind Streams*, *Geophys. Monogr. Ser.*, vol. 167, edited by B. T. Tsurutani et al., AGU, Washington, D. C, 2006.
- 525 Park, S. H., England, S. L., Immel, T. J., Frey, H. U., and Mende, S. B.: A method for determining the drift velocity of plasma depletions in the equatorial ionosphere using far - ultraviolet spacecraft observations, *J. Geophys. Res.*, 112, A11, <https://doi.org/10.1029/2007/JA012327>, 2007.
- Pi, X., A. J. Mannucci, U. J. Lindqwister, and C. M. Ho.: Monitoring of global ionospheric irregularities using the worldwide GPS network, *Geophys. Res. Lett.*, 530 24,18, 2283–2286, <https://doi.org/10.1029/97GL02273>, 1997.
- Pimenta, A. A., Fagundes, P. R., Bittencourt, J. A., Sahai, Y., Gobbi, D., Medeiros, A. F., Taylor, M. J., and Takahashi, H.: Ionospheric plasma bubble zonal drift: a methodology using oi 630 nm all-sky imaging systems, *Advances in Space Research.*, 27, 1219-1224, [https://doi.org/10.1016/s0273-1177\(01\)00201-0](https://doi.org/10.1016/s0273-1177(01)00201-0), 2001.
- 535 Patra, A. K., Chaitanya, P. P., Dashora, N., Sivakandan, M., and Taori, A.: Highly localized unique electrodynamic and plasma irregularities linked with the 17 march 2015 severe magnetic storm observed using multitechnique common - volume observations from gadanki, india, *J. Geophys. Res.*, 121,518-11,527, 540 <https://doi.org/10.1002/2016JA023384>, 2016.
- Sahai, Y., Becker-Guedes, F., Fagundes, P. R., de Jesus, R., de Abreu, A. J., Otsuka, Y., Shiokawa, k., Igarashi, K., Yumoto, K., Huang, C. S., Lan, H. T., Saito, A., Guarnieri, F. L., Pillat, V. G., and Bittencourt, J. A.: Effects observed in the ionospheric F region in the east Asian sector during the intense geomagnetic disturbances in the early part of November 2004, *J. Geophys. Res.*, 114, A00A18, 545 <https://doi.org/10.1029/2008JA013053>, 2009.

- Santos, A. M., Abdu, M. A., Souza, J. R., Sobral, J. H. A., Batista, I. S., and Denardini, C. M.: Storm time equatorial plasma bubble zonal drift reversal due to disturbance Hall electric field over the Brazilian region, *J. Geophys. Res.*, 121, 5594–5612, 550 <https://doi.org/10.1002/2015JA022179>, 2016.
- Sheehan, R. E., and Valladares, C. E.: Equatorial ionospheric zonal drift model and vertical drift statistics from UHF scintillation measurements in South America, *Ann. Geophys.*, 22, 3177–3193, <https://doi.org/10.5194/angeo-22-3177-2004>, 2004.
- 555 Scherliess, L., and Fejer, B. G.: Storm time dependence of equatorial disturbance dynamo zonal electric fields, *J. Geophys. Res.*, 102, 24037–24046, <https://doi.org/10.1029/97ja02165>, 1997.
- Taylor, M. J., Eccles, J. V., Labelle, J., and Sobral, J. H. A.: High resolution oi (630 nm) image measurements of f - region depletion drifts during the guará 560 campaign, *Geophys. Res. Lett.*, 24, 1699-1702, <https://doi.org/10.1029/97g101207>, 2013.
- Tulasi, R. S., Rama, R. P. V. S., Prasad, D. S. V. V. D., Niranjana, K., Gopi, K. S., and Sridharan, R.: Local time dependent response of postsunset esf during geomagnetic storms, *J. Geophys. Res.*, 113, A07310, 565 <https://doi.org/10.1029/2007/JA012922>, 2008.
- Weber, E., Buchau, J., and Moore, J.: Airborne studies of equatorial F layer ionospheric irregularities, *J. Geophys. Res.*, 85, 4631–4641, <https://doi.org/10.1029/JA085iA09p04631>, 1980.
- Xiong, C., Park, J., Lühr, H., Stolle, C., and Ma, S.Y.: Comparing plasma bubble 570 occurrence rates at CHAMP and GRACE altitudes during high and low solar activity, *Ann. Geophys.*, 28, 1647-1658, <https://doi.org/10.5194/angeo-28-1647-2010>, 2010.
- Xiong, C., Lühr, H., and Fejer, B. G.: Global features of the disturbance winds during storm time deduced from CHAMP observations, *J. Geophys. Res.*, 120, 5137– 575 5150, <https://doi.org/10.1002/2015JA021302>, 2015.

- Xiong, C., Stolle, C., Lühr, H., Park, J., Fejer, B. G., and Kervalishvili, G. N.: Scale analysis of the equatorial plasma irregularities derived from Swarm constellation, *Earth Planets Space.*, 68, 121, <https://doi.org/10.1186/s40623-016-0502-5>, 2016.
- Xiong, C., Xu, J., Wu, K., and Yuan, W.: Longitudinal thin structure of equatorial plasma depletions coincidentally observed by swarm constellation and all-sky imager, *J. Geophys. Res.*, 123, 3, <https://doi.org/10.1002/2017JA025091>, 2018.
- 580 Wu, K., Xu, J., Wang, W., Sun, L., Liu, X., and Yuan, W.: Interesting equatorial plasma bubbles observed by all-sky imagers in the equatorial region of China, *J. Geophys. Res.*, 122, <https://doi.org/10.1002/2017JA024561>, 2017.
- 585 Wu, K., Xu, J., Xiong, C., and Yuan, W.: Edge plasma enhancements of equatorial plasma depletions observed by all-sky imager and the C/NOFS satellite, *J. Geophys. Res.*, 123, 8835-8849, <https://doi.org/10.1029/2018JA025809>, 2018.
- Yang, Z., Song, S., Jiao, W., Chen, G., and Xue, J.: Ionospheric tomography based on gnss observations of the cmonoc: performance in the topside ionosphere, *GPS Solutions.*, 21, 363-375, <https://doi.org/10.1007/s10291-016-0526-0>, 2016.
- 590 Zhang, R., Liu, L., Chen, Y., and Le, H.: The dawn enhancement of the equatorial ionospheric vertical plasma drift, *J. Geophys. Res.*, 120, 688-697, <https://doi.org/10.1002/2015JA021972>, 2015.
- Zhang, R., Liu, L., Le, H., and Chen, Y.: Evidence and effects of the sunrise enhancement of the equatorial vertical plasma drift in the F region ionosphere, *J. Geophys. Res.*, 121, 4826-4834, <https://doi.org/10.1002/2016JA022491>, 2016.
- 595 Zheng, J., Zhao, B., Xiong, B., and Wan, W.: Spatial and temporal analysis of the total electron content over china during 2011-2014, *Advances in Space Research.*, 57, 12, <https://doi.org/10.1016/j.asr.2016.03.037>, 2016.
- 600 Zhou, Y. L., Lühr, Hermann, Xiong, C., and Pfaff, R. F.: Ionospheric storm effects and equatorial plasma irregularities during the 17-18 march 2015 event, *J. Geophys. Res.*, 121, 9146-9163, <https://doi.org/10.1002/2016JA023122>, 2016.

Figure Captions

Figure 1. The location of observation instruments. The red star denotes the geographic location of the all-sky imager at Qujing (25° N, 104° E). The blue circle denotes the field of view of the all-sky imager at an altitude of 250 km. The green dot denotes the geographic location of the digisonde at Fuke (19.5° N, 109.1° E). The red dotted line represents the magnetic equator.

Figure 2. (a) Kp indexes, (b) the interplanetary magnetic field (IMF) B_z , (c) SYM/H, and (d) AE, AU, AL during 06-08 November 2015. (e) The variations of h'F obtained from the digisonde at Fuke on 06-08 November 2015.

Figure 3. Images of equatorial plasma bubbles from the Qujing site between 05:15 LT and 06:21 LT on 08 November 2015. The observed images were mapped into geographical coordinates by assuming that the airglow emission layer was at an altitude of ~250 km. The white vertical line is a reference line of 106° E and horizontal line is a reference line of 25° N.

Figure 4. Total electron content residuals over China and adjacent areas with 10 minute interval during 04:30 – 08:20 LT on 08 November 2015. The black horizontal line is a reference line of 25° N.

Figure 5. Two-dimensional map of absolute TEC during 05:15 – 08:00 LT on 08 November 2015.

Figure 6. Two-dimensional map of rate of TEC index (ROTI) correspond to each image of Figure 3. The black horizontal line is a reference line of 25° N. The black vertical line is a reference line of 106° E.

Figure 7. (a) N-S cross sections (between 104°E and 105°E) of the airglow images on

08 November 2015. (c) W-E cross sections (between 21.5°N and 22°N) of the airglow images. (e) W-E cross sections (between 18.5°N and 19°N) of the airglow images. (b) The variations of the meridian velocities of “b1” with local time. (d) and (f) The variations of the zonal velocities of “b1” at ~ 22°N and ~19°N geographical latitudes, respectively.

Figure 8. Contours of nighttime zonal winds at 250 km in a range from 0° to 40° N in latitude and from 90° to 120° E in longitude during 08 November 2015. The dashed rectangles represent the location of EPBs.

Figure 9. The ionograms observed by the digisonde at Fuke between 04:00 LT and 07:30 LT on 08 November 2015.

Figure 10. The height of hmF2 in a range from 0° to 40° N in latitude and from 90° to 120° E in longitude during 08 November 2015. The red star represent the location of all-sky imager. The dashed rectangles represent the region of southeastern Qujing.

Figure 1

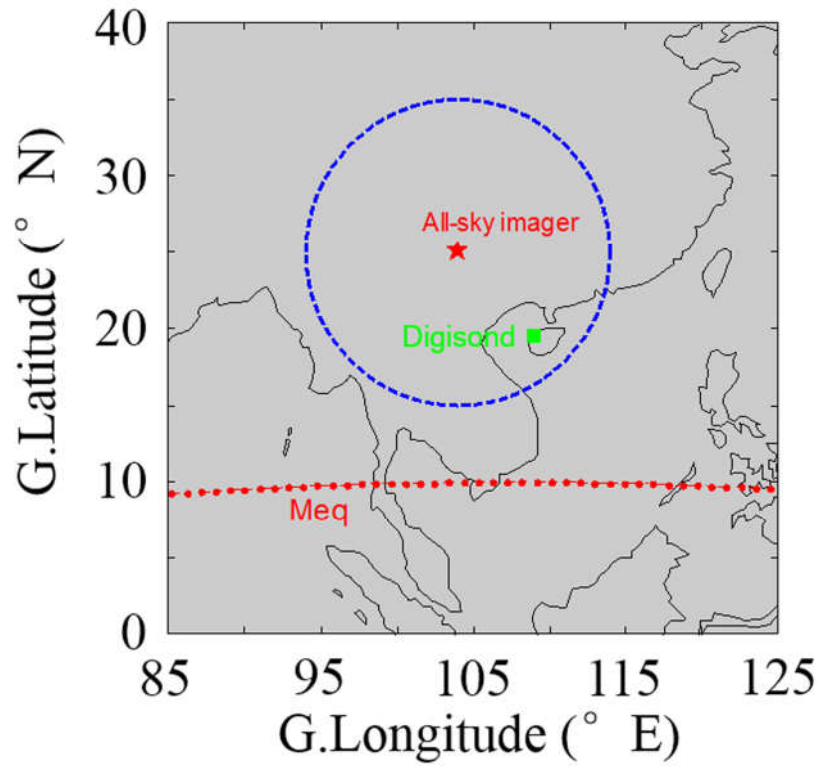


Figure 2

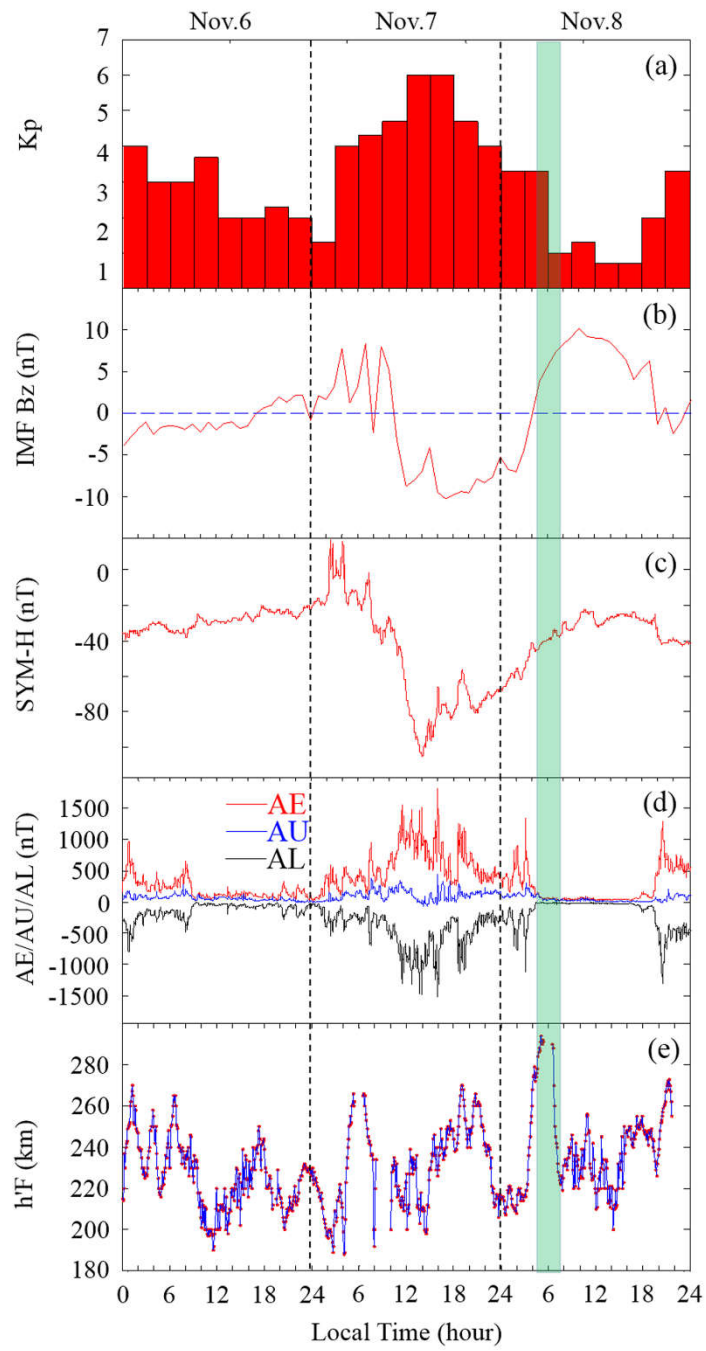


Figure 3

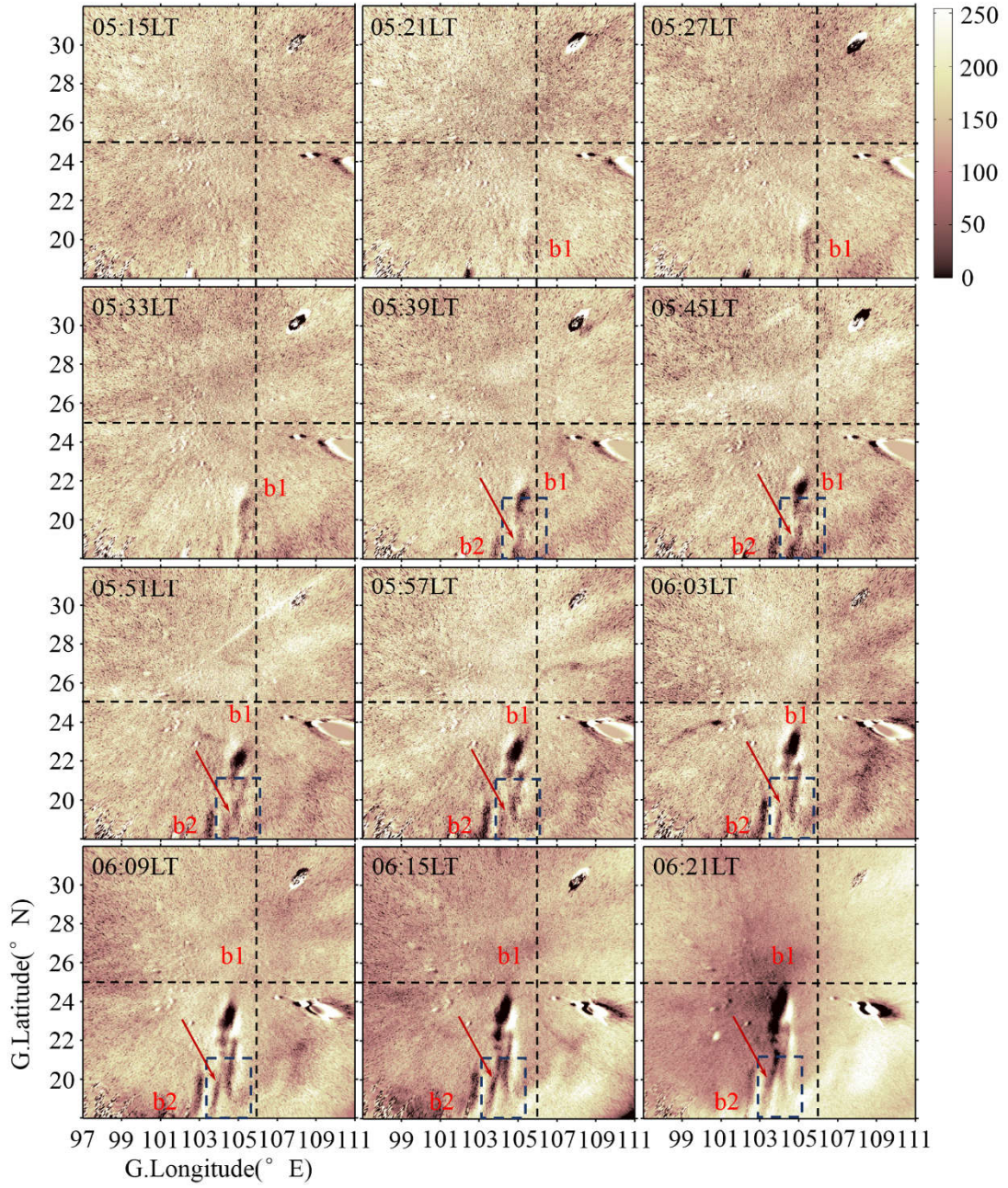


Figure 4

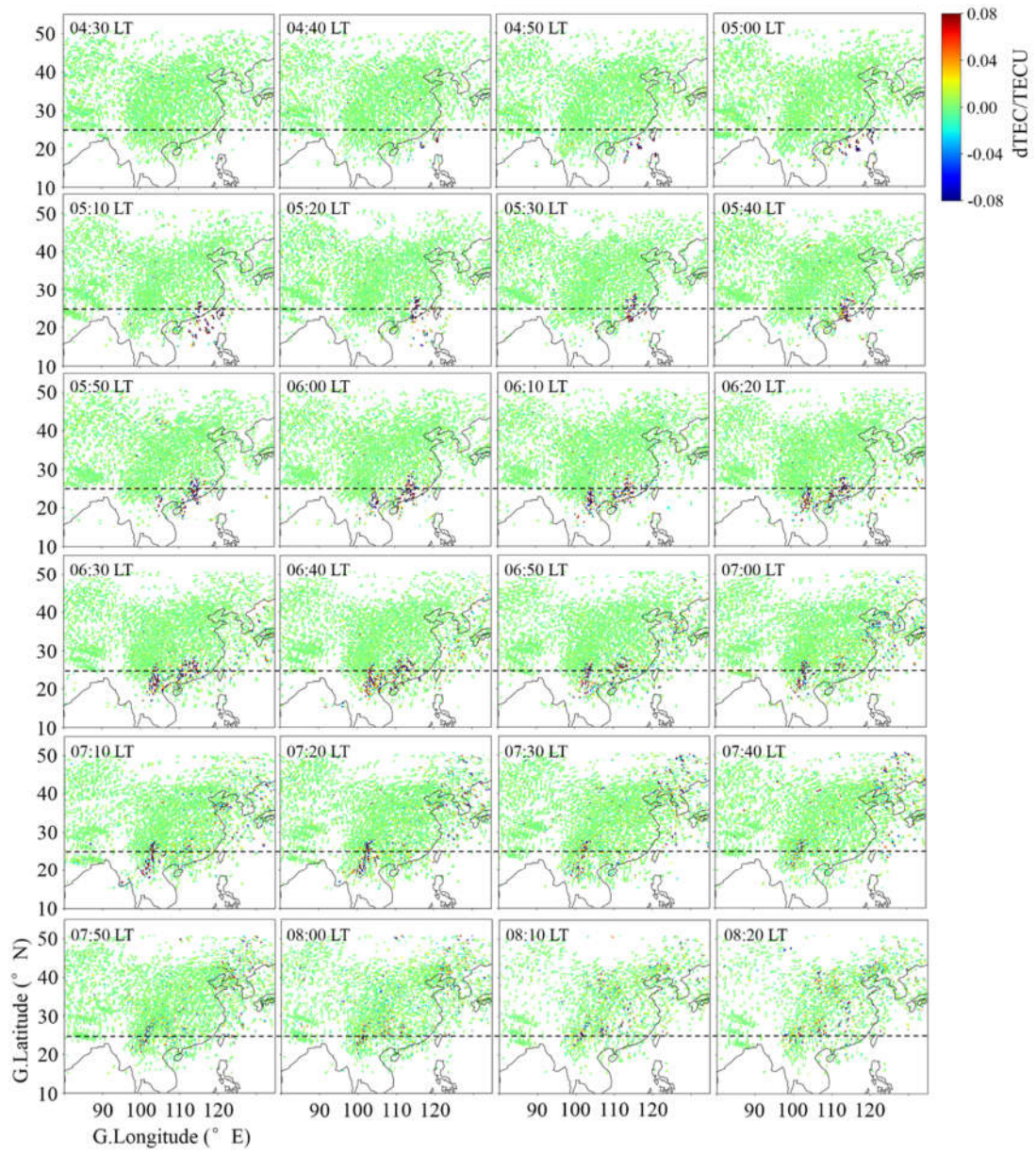


Figure 5

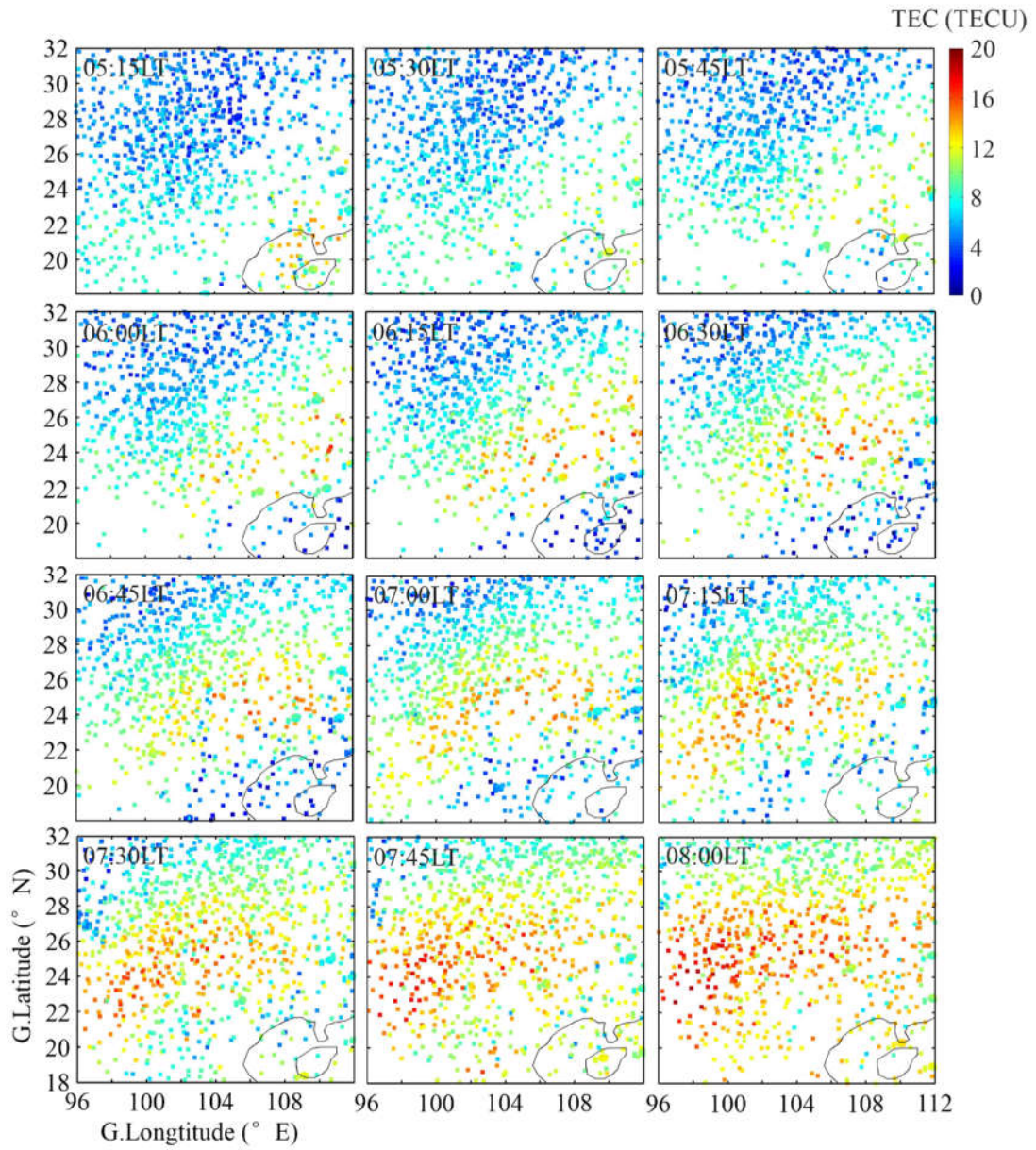


Figure 6

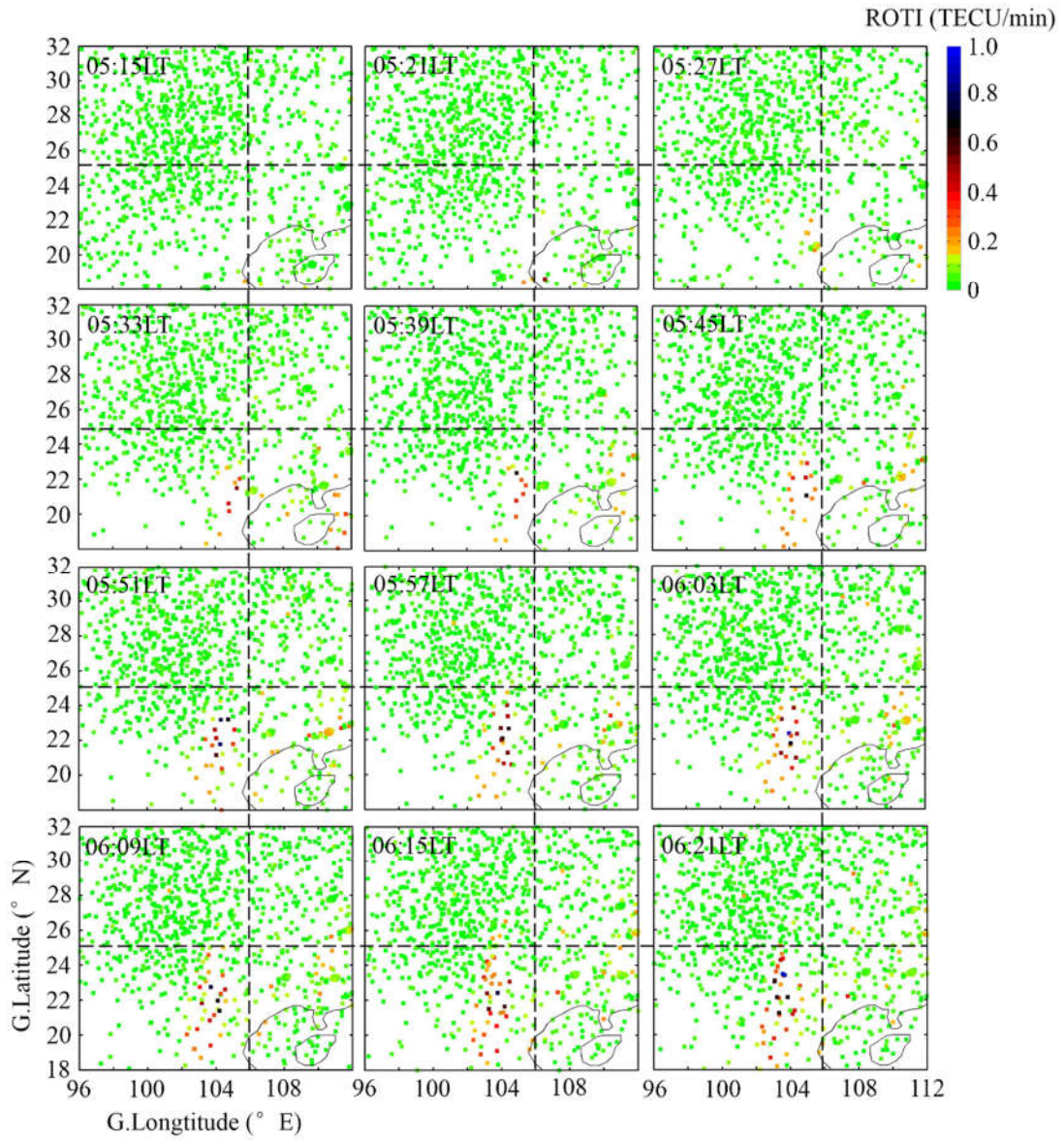


Figure 7

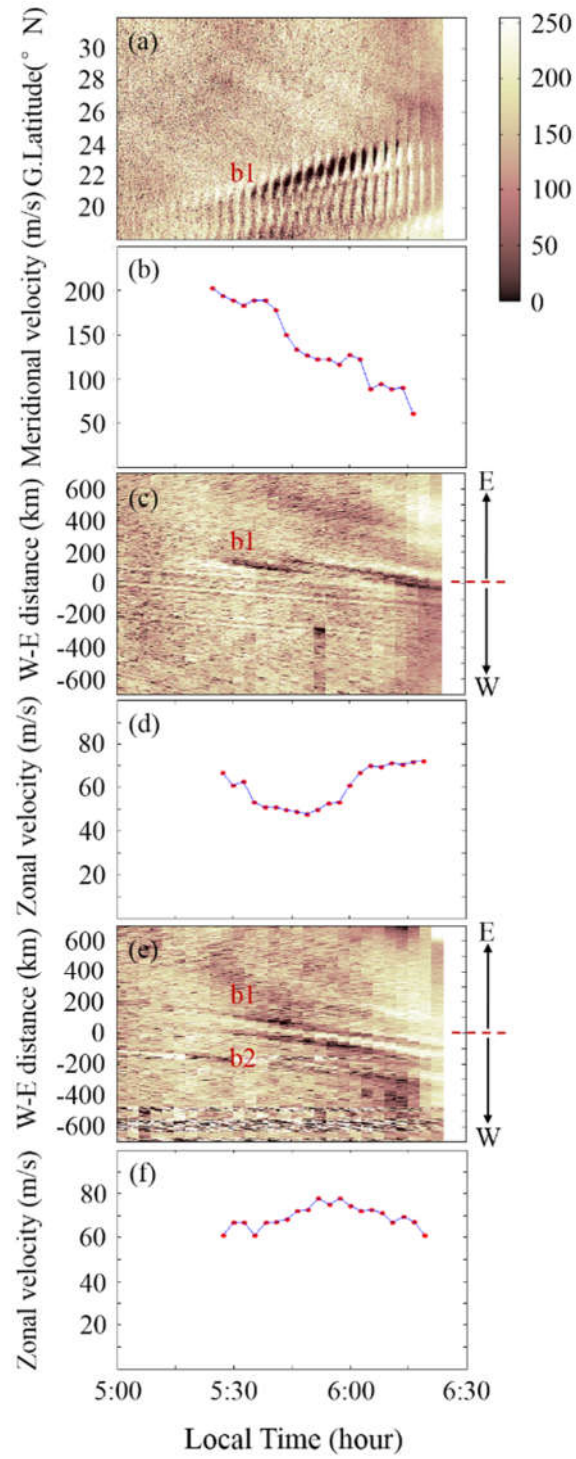


Figure 8

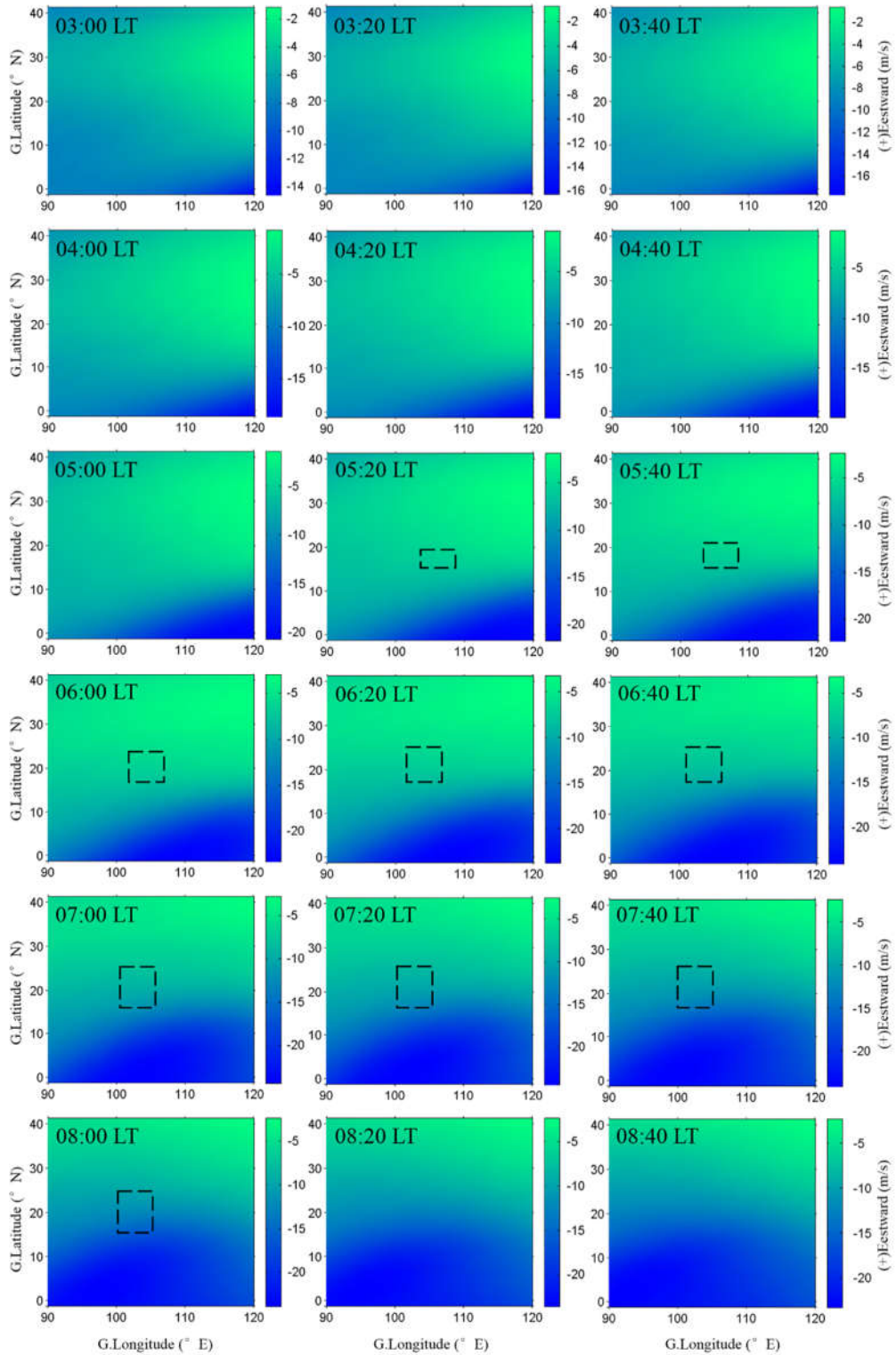


Figure 9

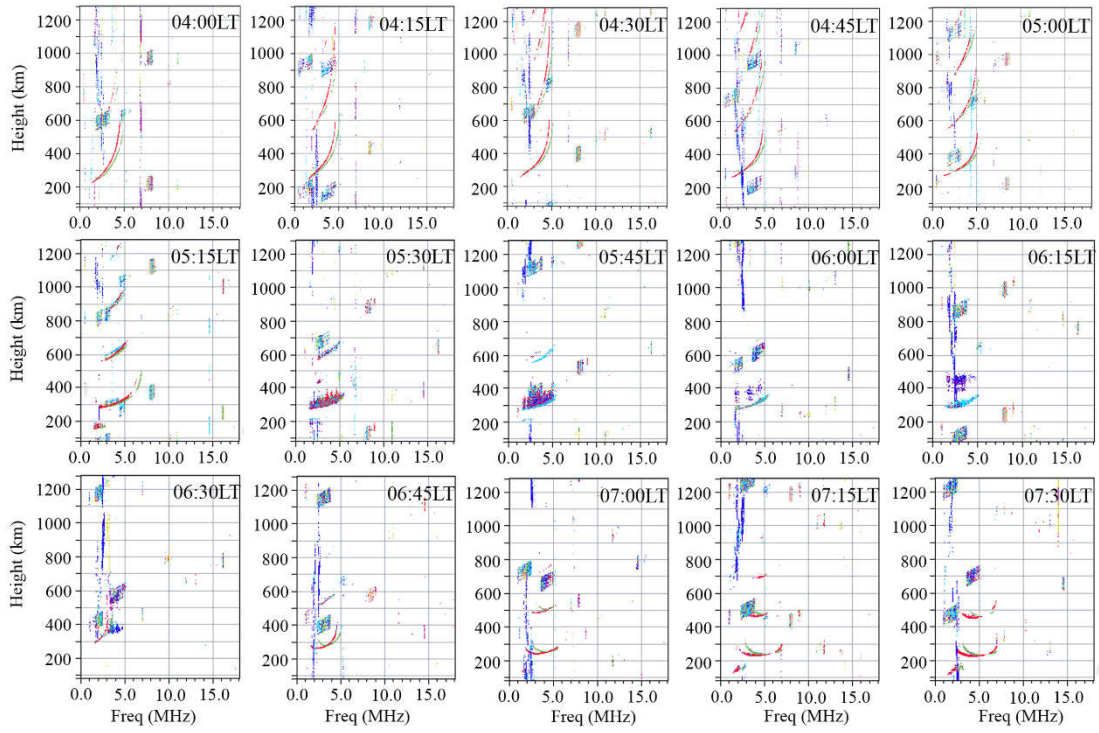


Figure 10

